Engineering 25 (2023) 214–221

Contents lists available at ScienceDirect

Engineering

journal homepage: www.elsevier.com/locate/eng

Research
Environmental Engineering—Article

Persulfate-Induced Three Coordinate Nitrogen ($N3_C$) Vacancies in Defective Carbon Nitride for Enhanced Photocatalytic H_2O_2 Evolution

Wei Miao [a,b], Yijie Wang [a,b], Ying Liu [a,b], Hehe Qin [a,b], Chengcheng Chu [a,b], Shun Mao [a,b,*]

[a] College of Environmental Science and Engineering, Biomedical Multidisciplinary Innovation Research Institute, Shanghai East Hospital, State Key Laboratory of Pollution Control and Resource Reuse, Tongji University, Shanghai 200092, China
[b] Shanghai Institute of Pollution Control and Ecological Security, Shanghai 200092, China

ARTICLE INFO

Article history:
Received 10 August 2021
Revised 3 December 2021
Accepted 16 December 2021
Available online 25 February 2022

Keywords:
Carbon nitride
$N3_C$ vacancy
Hydrogen peroxide evolution
Photocatalysis
Persulfate

ABSTRACT

In-situ photocatalytic H_2O_2 production has been receiving increasing attention in recent years for sustainable H_2O_2 synthesis. Graphitic carbon nitride (g-C_3N_4) is regarded as one of the most promising semiconductor photocatalysts for H_2O_2 evolution. Introducing N defects in g-C_3N_4 has been proved to be an effective strategy to enhance photocatalytic activity. However, the photocatalytic mechanism of the N vacancies is ambiguous and different types of N vacancies in g-C_3N_4 may exhibit different effects on photocatalytic activity. Herein, we develop a facile sodium persulfate eutectic polymerization method to prepare the g-C_3N_4 with abundant three coordinate nitrogen ($N3_C$) vacancies. This type of nitrogen vacancy has not been studied in g-C_3N_4 for photocatalytic H_2O_2 production. Our results show that the introduction of $N3_C$ vacancies in the g-C_3N_4 successfully broadens the light absorption range, and inhibits the photoexcited charge recombination with enhanced O_2 adsorption to promote oxygen activation. The photocatalytic H_2O_2 evolution from the $N3_C$-rich g-C_3N_4 is 4.5 times higher than that of the pristine g-C_3N_4. This study demonstrates a novel strategy to introduce $N3_C$ vacancies in g-C_3N_4, which offers a new method to develop active catalysts for photocatalytic H_2O_2 evolution.

1. Introduction

Hydrogen peroxide (H_2O_2) is one of the most valuable chemicals in pharmaceutical, chemical, food, and environmental industries [1–3]. It is a potential oxidant for carbonaceous fuels in electricity generation [4]. The traditional large-scale production of H_2O_2 relies on the energy-intensive anthraquinone method [5]. The sustainable *in-situ* production of H_2O_2 can significantly reduce the production, storage, and transportation costs with minimized safety risks [6]. Recently, sunlight-driven H_2O_2 generation using suitable photocatalysts has become a research hotspot [7,8]. Various photocatalysts including metal oxides (TiO_2 and $BiVO_4$) [9,10], metal–organic materials (MOMs) [11], metal-free polymers [12], and graphitic carbon nitride (g-C_3N_4) have been studied for the photocatalytic H_2O_2 production [13,14]. Among those semiconductors, g-C_3N_4 is considered a promising photocatalyst owing to the merits of suitable bandgap structure, good thermal and chemical stability, low cost with facile production process [15–18]. However, pristine g-C_3N_4 only offers a limited visible-light absorption range. It suffers from rapid charge recombination and low charge carrier mobility with a poor selectivity towards the two-electron ($2e^-$) reaction pathway. Therefore, further enhancement of the photocatalytic activity of g-C_3N_4 in H_2O_2 production becomes a hot research topic in recent years.

Introducing defects (nitrogen and carbon vacancies) in g-C_3N_4 was reported to be effective in enhancing photocatalytic H_2O_2 production [19,20]. Specifically, N vacancies engineering in g-C_3N_4 can not only adjust the bandgap structures for harnessing more visible light but also increase the surface energy to promote active sites for oxygen reduction [21]. For instance, with KOH-assisted polymerization of the nitrogen-rich precursors, nitrogen defects and the cyano group were introduced into the g-C_3N_4 to control the band structure. As the electron-withdrawing groups, nitrogen defects, and cyano groups could improve the charge transportation to delivery charges to the surface terminal sites [22,23]. In addition to KOH, other K or Na salts have also been used to modify g-C_3N_4 to enhance the production of H_2O_2 via two specific mechanisms, that is, modifying the pre-synthesized g-C_3N_4 or participating in the molten polymerization synthesis of g-C_3N_4 [24–28]. The

* Corresponding author.
E-mail address: shunmao@tongji.edu.cn (S. Mao).

https://doi.org/10.1016/j.eng.2021.12.016

advantages of the alkali-assisted modification method can be summarized as follows: ① The generated N vacancies inhibit the charge recombination; ② the coexistence of cyano groups and N vacancies affects the bandgap of g-C_3N_4; ③ introduction of alkali metal dopants broadens the light absorption range; and ④ the incorporation of multiple hetero-elements (O, S, P) into the polymeric CN matrix enhances the charge transfer properties. Although this method can introduce N vacancies in g-C_3N_4, the formation and identification of nitrogen defects have not received enough attention. Moreover, different types of N vacancies produced in this method may exhibit different photocatalytic performances. Recently, g-C_3N_4 containing two types of N vacancies (NH_x and $N2_C$) has been reported, where NH_x promotes the photoexcited charge separation and $N2_C$ is responsible for the oxygen activation [29]. $N3_C$ vacancy is another type of N vacancy that has been reported in photocatalytic NO_x reduction and H_2 production [30,31], which has yet been studied in photocatalytic H_2O_2 production.

Herein, we designed a one-step sodium persulfate (PDS)-assisted molten polymerization method to produce g-C_3N_4 with $N3_C$ vacancies. The effects of N vacancies and defects in g-C_3N_4 in photocatalysis were characterized by investigating the light absorption performance, charge transfer properties, and the selective two-electron pathway. Importantly, the process and mechanism of PDS-induced formation of $N3_C$ vacancy during the polymerization process were also elucidated. The H_2O_2 evolution study showed that g-C_3N_4 with the highest amount of $N3_C$ offered the best H_2O_2 evolution activity, which is 4.5 times higher than that of the pristine g-C_3N_4. To the best of our knowledge, this is the first time to identify the role of the $N3_C$ vacancy in g-C_3N_4 for promoting the photocatalytic production of H_2O_2. The reported sodium persulfate-assisted synthetic method provides a novel strategy to customize $N3_C$ vacancies in g-C_3N_4 and has significant implications for developing photocatalysts for other applications.

2. Experimental

2.1. Chemicals

Sodium persulfate ($Na_2S_2O_8$, 99.0%) and *p*-Benzoquinone (*p*-BQ, 99.0%) were purchased from Aladdin Chemistry Co., China. Melamine, ethanol (analytical reagent (AR), 95.0%), and sodium sulfate (Na_2SO_4) were supplied by Macklin Biochemical Co., Ltd. (China). Ethanol (99.5%) and potassium iodide (KI) were obtained from Sinopharm Chemical Reagent Co., Ltd. (China). Methanol (MeOH, high performance liquid chromatography (HPLC)) and isopropanol (IPA, HPLC) were bought from Anpel Laboratory Technologies Inc., China. Ultrapure water (18.2 MΩ·cm^{-1}) produced from Milli-Q System was used in all experiments.

2.2. Preparation of the catalysts

Before the synthesis, 10 g melamine was mixed with 0.33 mol $Na_2S_2O_8$ followed by grounding for 30 min to form a uniform precursor. This mixture was heated to 550 °C in an Ar atmosphere at a heating rate of 5 °C·min^{-1} and kept for 2 h. The obtained solid was ground and washed with ultrapure water before being dried at 60 °C. The obtained sample was named sodium persulfate doped g-C_3N_4 (SPCN). The sodium sulfate doped g-C_3N_4 (SSCN) was prepared by the same method with 10 g melamine mixed with 0.33 mol of sodium sulfate (Na_2SO_4). The pristine g-C_3N_4 (CN) was prepared by the same method with only melamine as the precursor.

2.3. Characterizations

X-ray diffraction (XRD) patterns were collected on a Bruker D8-Advanced X diffractometer (Germany) with Cu–Kα radiation. Fourier transform infrared spectroscopy (FTIR) spectra were acquired on a Nicolet 380 spectrometer (USA). The microstructure of the samples was characterized using a scanning electron microscope (SEM; Hitachi S-4800, Japan). X-ray photoelectron spectroscopy (XPS) study was conducted by a Thermo Scientific K-Alpha spectroscope (USA). Thermogravimetry analysis (TGA) was measured on an FEI Themis Z (USA), and the sample was heated at a rate of 10 °C·min^{-1} up to 550 °C under Ar atmosphere (30 mL·min^{-1}). Ultraviolet–visible diffuse reflectance spectra (UV–vis DRS) were collected on a UV-2450 spectrophotometer (Shimadzu, Japan) equipped with an integrating sphere with $BaSO_4$ as the reference. The O_2 temperature-programmed desorption (TPD) measurement was performed on a Thermo Scientific ESCALAB XI+. Electron paramagnetic resonance (EPR; Bruker A300-10/12) was performed to detect the nitrogen vacancy. The photoluminescence (PL) emission spectra were obtained on a Hitachi F-7000 fluorescence spectrophotometer at an excitation wavelength of 355 nm. The zeta potentials of the prepared samples were measured by a Zetasizer Nano ZS90 analyzer (China). The setup of a photoelectrochemical reactor is shown in Text S1 in Appendix A.

2.4. Photocatalytic H_2O_2 evolution

H_2O_2 evolution tests were conducted in a photocatalytic reactor. Typically, 25 mg photocatalyst was dispersed into 50 mL of isopropanol/H_2O mixture (10/90, v/v). The suspension was stirred and ultrasonicated for 5 min. A 300 W white-light light emitting diode (LED; CEL-PE300-4A; AuLight, China) with a 420 nm cutoff filter was used as the light source with a light intensity of 100 mW·cm^{-2} (at the upper surface of the solution). During the reaction, the solution was stirred continuously without pumping in O_2. The solution was sampled every 10 min, which was filtered using a 0.22 μm Millipore filter. The concentration of H_2O_2 was determined by iodometric titration with a UV–vis spectrophotometer (see details in Fig. S1 in Appendix A) [32].

3. Results and discussion

3.1. Structure and chemical composition of the catalyst

As shown in Fig. S2 in Appendix A, SSCN and SPCN have similar morphologies to pristine CN. However, porous structure and rough surface were observed due to the etching by Na_2SO_4/$Na_2S_2O_8$ eutectic salts during the thermal treatment [27]. The XRD patterns (Fig. 1(a)) of all prepared carbon nitride samples show two characteristic peaks at 13.2° and 27.0°, which are assigned to the (100) and (002) crystal planes of g-C_3N_4, respectively. Compared with pristine CN, both peaks were weakened with the addition of Na_2SO_4 or $Na_2S_2O_8$. This weakening in XRD suggests the reduction of ordering in the tri-*s*-thiazine units (100) and the interlayer (002) stacking [33]. There are no other peaks from sodium or sulfur were observed in the XRD patterns due to the extremely low content of sodium and sulfur. However, weak Na 1s signals were identified in the XPS survey spectra from SSCN and SPCN (Fig. S3 in Appendix A). The surface element contents of the different samples are listed in Table S1. The result indicates that no sulfur species were left in the polymeric CN products. As shown in the FTIR spectra (Fig. 1(b)), multiple peaks between 900 and 1800 cm^{-1} were assigned to the stretching of the melon structural unit (N–C=N) in the aromatic heterocycles. With the addition of sodium salts in the synthesis, the intensities of the breathing mode of the tri-*s*-triazine at

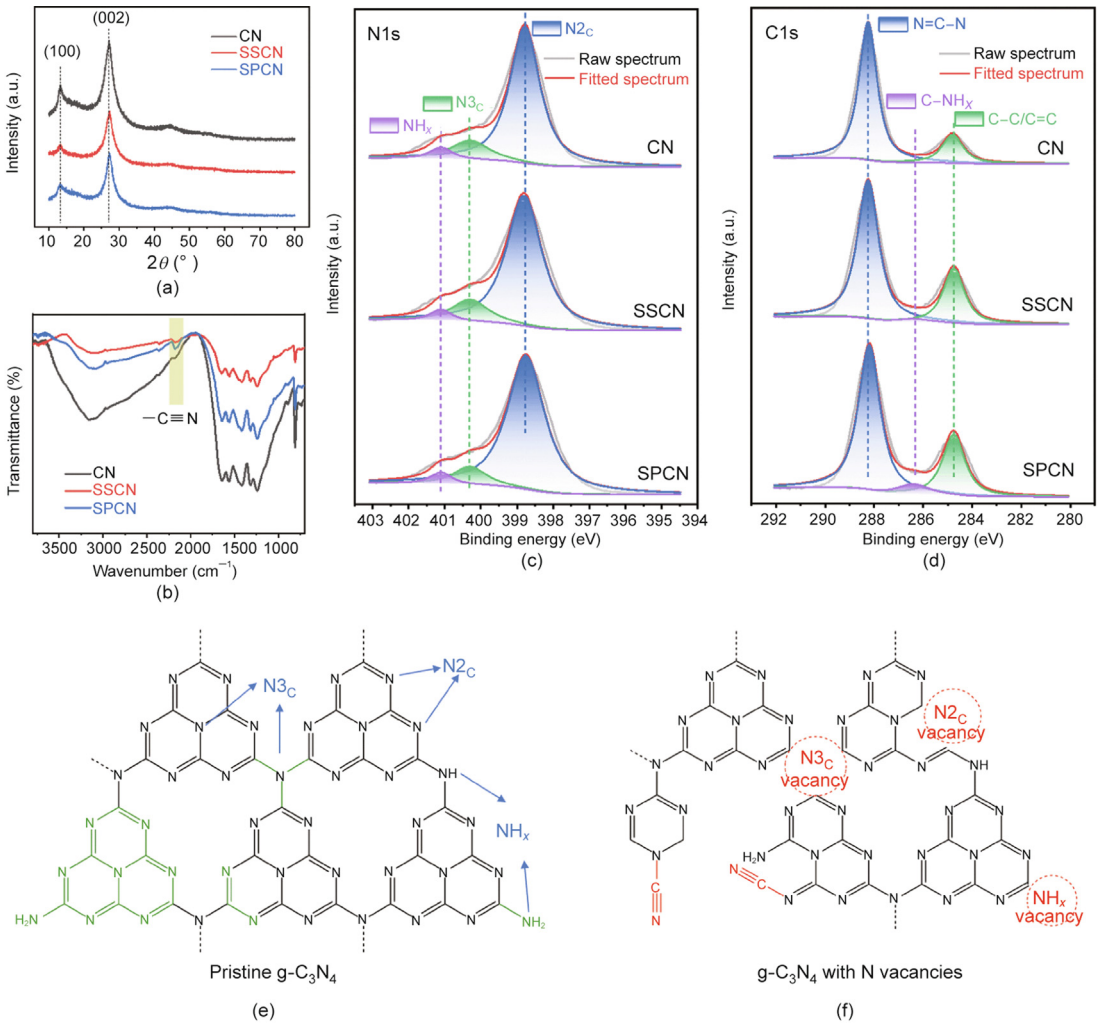

Fig. 1. Chemical composition of as-synthesized photocatalysts. (a) XRD patterns, (b) FTIR spectra, (c) XPS N1s spectra, and (d) XPS C1s spectra of CN, SSCN, and SPCN. The schematic illustrations of N groups (blue) in (e) pristine g-C_3N_4, and (f) the N vacancies (red) in modified g-C_3N_4.

810 cm^{-1} and the stretching of $-NH_x$ groups as the broad peaks between 3000–3500 cm^{-1} were decreased. Meanwhile, a new peak at 2177 cm^{-1} corresponding to cyano groups (−C≡N) emerged, which was formed by the deprotonation of the terminal –C–NH_2.

The N/C and O/C atomic ratios were measured (Table S1) to further investigate the effects of $Na_2S_2O_8$ modification on g-C_3N_4. Compared with pristine CN, the O/C ratios for both SSCN and SPCN are both increased, accompanied by the decrease in the N/C ratio. Similar O/C ratios are detected for SSCN and SPCN, indicating that sodium persulfate does not introduce more oxygens into the CN framework than sodium sulfate. Considering that the formation of cyano groups does not affect the N contents, other forms of defects, such as N vacancies, must be produced with the addition of $Na_2S_2O_8$ or $Na_2S_2O_8$. SPCN has the lowest N/C ratio, which is expected to have the highest density of N defects [22]. To confirm the origin of N defects, the high-resolution XPS spectra of N1s and C1s are analyzed (Figs. 1(c) and (d)). Fig. 1(c) shows that the N1s region is formed by three characteristic peaks including the sp^2 hybridized aromatic nitrogen (C–N=C, $N2_C$) at 398.8 eV, the tertiary nitrogen (N–(C)3, $N3_C$) at 400.3 eV, and the uncondensed amino groups N–H_x (x = 1, 2) at 401.1 eV [34]. It is noticed that the decrease of the N content in the modified CN manifests the generation of N vacancies as shown in Figs. 1(e) and (f). As listed in Table 1, the relative compositions of $N3_C$ and NH_x were decreased along with the increase of $N2_C$ for the SPCN sample, which reveals that more $N3_C$ vacancies were produced rather than the $N2_C$ vacancies [29]. The content of $N3_C$ in SPCN is 10.14%, which is lower than that of CN (14.10%) and Na_2SO_4 (14.08%), indicating that the persulfate induces a large amount of $N3_C$ vacancies in SPCN.

As shown in Fig. 1(d), the C1s region of the pristine CN was deconvoluted into two characteristic peaks of C–C bonds at 286.4 eV and sp^2 carbon (N=C–N) at 288.1 eV [35]. A new peak corresponding to the C≡N or C–NH_x appears at 286.4 eV for the modified CN [28]. The intensity of the 286.4 eV peak in SPCN is higher than that in SSCN. Based on the XPS results of N1s, the content of NH_x is similar in SSCN and SPCN. Therefore, the extra peak intensity at 286.4 eV is associated with the higher C≡N content in SPCN than in SSCN, providing additional evidence for a higher amount of cyano groups shown in the FTIR spectra in Fig. 1(b).

3.2. Formation of $N3_C$ defects

To study the phase transformation during the eutectic crystallization of persulfate and melamine, thermogravimetry-derivate thermogravimetric (TG/DTG) measurement was performed to simulate the thermal environment of the synthesis process. As shown in the inset of Fig. 2(a), there is no weight loss before 210 °C, although the decomposition temperature of persulfate is 180 °C.

Table 1
The contents of N and C coordination groups in the catalysts estimated by XPS results.

Catalyst	N coordination type content (%)			C coordination type content (%)		
	$N2_C$ 398.8 eV	$N3_C$ 400.3 eV	NH_x 401.1 eV	C–C 284.6 eV	C≡N or C–NH_x 286.4 eV	N=C–N 288.1 eV
CN	80.96	14.10	4.93	19.06	–	80.94
SSCN	81.80	14.08	4.11	27.68	2.34	69.98
SPCN	85.73	10.14	4.13	28.05	6.28	65.67

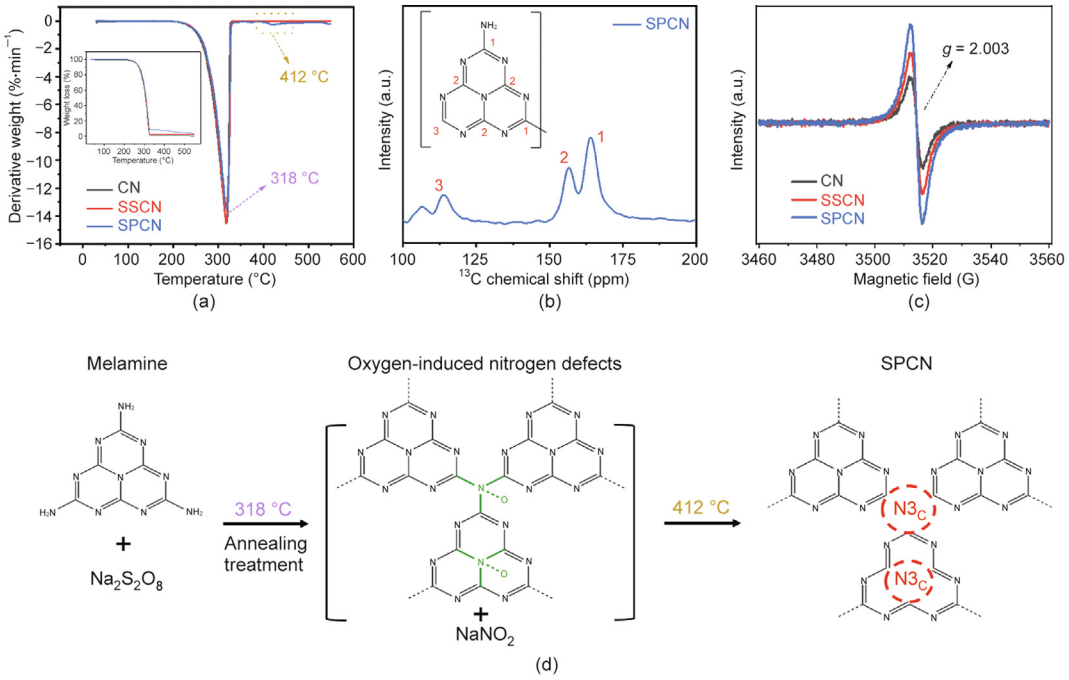

Fig. 2. The formation of $N3_C$ vacancies during the polymerization process of SPCN. (a) TG/DTG curves of the prepared catalysts. (b) Solid-state ^{13}C NMR spectra of SPCN. (c) EPR spectra of the prepared catalysts. (d) The speculated formation route of $N3_C$ vacancies during the persulfate-assisted molten polymerization process of CN. ppm: parts per million.

The improved thermal stability may be due to the synergistic effect of electrostatic and hydrogen bonding interaction between the O–O (Na_2SO_3–O–O–SO_3) bond and –NH_2 groups of melamine [36,37]. The rapid weight loss peak appeared at the temperature between 210 and 318 °C, associated with the deamination, sublimation, and thermal condensation of melamine [38]. Among them, melamine doped by persulfate showed the least weight loss due to the aforementioned synergistic stabilization effect inhibiting the release of NH_3 and the degree of condensation. Meanwhile, melamine doped by sodium sulfate showed less weight loss than pure melamine. Additionally, eutectic Na salts could improve the mass transport of the reactants and achieve a more uniformly distributed dopant in carbon nitride [24]. Notably, there is another weight loss peak at a higher temperature of 412 °C only in the persulfate doped melamine sample, implying a further polymerization to generate small molecule fragments containing oxygen and nitrogen. Compared with the typical phase formation from melamine to g-C_3N_4, this process forms more cyano and nitrogen vacancies.

Solid-state ^{13}C nuclear magnetic resonance (NMR) spectroscopy of SPCN showed two dominant peaks at 156.4 and 164.5 parts per million (ppm), which corresponds to the chemical shifts of C2N–NH_x (peak 2) and C3N (peak 1) in the heptazine units, respectively (Fig. 2(b)). This phenomenon indicates that the PDS-assisted eutectic polymerization process does not alter the main heptazine core structure [26]. Notably, a broad peak at 115.8 ppm assigned to the aromatic pyridine carbon species (peak 3) in the CN framework was observed, implying the formation of $N3_C$ vacancies [39]. Solid-state EPR spectra were collected to investigate the electronic band structure of nitrogen vacancies. As shown in Fig. 2(c), the Lorentz signal with g = 2.003 was recorded for all three samples, which is assigned to the unpaired electrons of the sp^2 hybridized carbon atoms on the π-conjugated planes of g-C_3N_4. The higher intensity in the EPR signal represents more unpaired electrons, associated with the higher population of nitrogen vacancies introduced by the thermal eutectic persulfate treatment [40]. Combining the EPR the XPS results, $N3_C$ vacancies were mainly introduced in SPCN. In this regard, a higher number of unpaired electrons can facilitate the photocatalytic H_2O_2 evolution reaction [41].

The zeta-potential analysis was used to further understand the surface properties of the catalysts. As shown in Fig. S4 in Appendix A, CN exhibits the zero-point charge (pH_{ZPC}) at pH 3. In contrast, the SSCN and the SPCN surfaces were negatively charged over the entire pH range from 2 to 9. This result indicates the electron-withdrawing ability of SPCN was enhanced due to the strong electronegativity of the N atoms in the C≡N and/or unsaturated C atoms surrounding the $N3_C$ defects [35,42]. SPCN showed a slightly positive zeta potential than SSCN at the same pH. Based on the element component analysis (Table S1), it can be inferred that the presence of positively charged Na^+ ions partially counteracted the negative charges on SPCN [43]. The more negatively charged surface of the photocatalyst can enhance the adsorption of O_2, which could subsequently react with H^+ to produce H_2O_2 [44].

The schematic illustration of the persulfate-induced surface modification during the synthesis of SPCN is shown in Fig. 2(d). At the first step of polymerization, the released N component was oxidized by the low eutectic salt sodium sulfite salt. In the second step, the oxygen species in the g-C_3N_4 framework were released to form sodium sulfate. As a consequence, this process generates more defects in SPCN compared to that in SSCN. As shown in Figs. 1(e) and (f), the potential reaction sites (green parts) on the pure CN can be converted into N defects (red parts) following the molten salt eutectic reaction. By summarizing the above observations, the presence of persulfate during the synthesis of g-C_3N_4 produced more active sites in the form of $N3_C$ vacancies and cyano groups for photocatalytic H_2O_2 evolution.

3.3. Band structure and optical properties

The light absorption properties are critical to photocatalytic H_2O_2 production performance. The UV–vis DRS absorption spectra in Fig. 3(a) show that the catalysts had good absorption in the visible region. Compared with CN, the adsorption edges of both the SPCN and the SSCN are redshifted, indicating improved visible light absorption. The broad increase of the absorption in the long wavelength by SSCN and SPCN indicates the more homogeneous distribution of N defects [22]. SPCN shows the highest absorption in the visible region, which is associated with its highest density of defects. Bandgap energy (E_g) of the samples was calculated using the Kubelka–Munk function (see details in Text S2 in Appendix A) based on the UV–vis DRS data [45]. The results show that the light-harvesting abilities were enhanced from the SSCN and the SPCN in comparison with the pristine CN due to the high population of N defects and cyano groups introduced during the thermal polymerization of melamine with the presence of eutectic sodium salt.

To identify the band edges of the catalysts, the work function and the valence band (VB) of the catalyst were determined by ultraviolet photoelectron spectroscopy (UPS) (Fig. 3(b) and Fig. S5 in Appendix A). The cut-off binding energy (E_C) of all samples was determined as 16.40 eV. Then, the work function (Φ) of the catalysts was calculated as 4.82 eV by $E_{He-I} - E_C$, where E_{He-I} (He–I photoelectron energy) is the photon energy (21.22 eV) [46]. The energy of VB (E_{VB}) of SPCN was determined to be 6.33 eV (vs vacuum) by $\Phi + E_{VB/HOMO}$ (HOMO: the highest occupied molecular orbital). With the E_g from the DRS results, the position of the conduction band (CB) of SPCN was calculated to be 3.68 eV by $E_{VB} - E_g$. Finally, the E_{VB} and E_{CB} of CN, SSCN, and SPCN were converted to the electrochemical potentials with respect to reversible hydrogen electrode (RHE) (−4.44 eV vs vacuum) [47]. The band alignments of the catalysts are shown in Fig. 3(c).

As shown in the photoluminescence (PL) spectra (Fig. 3(d)), the major peak around 465 nm is ascribed to the band–band recombination of photogenerated carriers. The fluorescence intensity of this peak is in the order of CN > SSCN > SPCN, which implies that the charge separation ability was improved with the sodium salts modification. It is also found that this peak was redshifted for the SPCN sample, associated with the reduction of the bandgap energy, which is consistent with the DRS results [44,48]. Moreover, as shown in Fig. 3(e), the decreased electrochemical impedance spectroscopy (EIS) slop of SPCN also reflects the improved charge migration rate and the reduced electric transferring resistance, which benefits the photoelectric activity [49]. Considering the above facts, this enhancement is attributed to the improved charge-trapping offered by the defect sites of cyano groups and N vacancies.

To further investigate the influence of N vacancies on photocatalytic performance, the transient photocurrent responses were obtained, which represented the efficiency of using the photogenerated electrons and holes in the redox reactions. Considering the aforementioned results of light-harvesting capability and charge separation efficiency, the order of photoelectric activity is as follows: SPCN > SSCN > CN. The stable photocurrent density of SPCN (plateau: 0.315 μA·cm^{-2}) under visible light irradiation is 1.56- and 3.12-fold higher than that of SSCN and CN, respectively (Fig. 3(f)). Therefore, the introduction of $N3_C$ vacancies is beneficial to the charge separation of g-C_3N_4. Due to the presence of extra

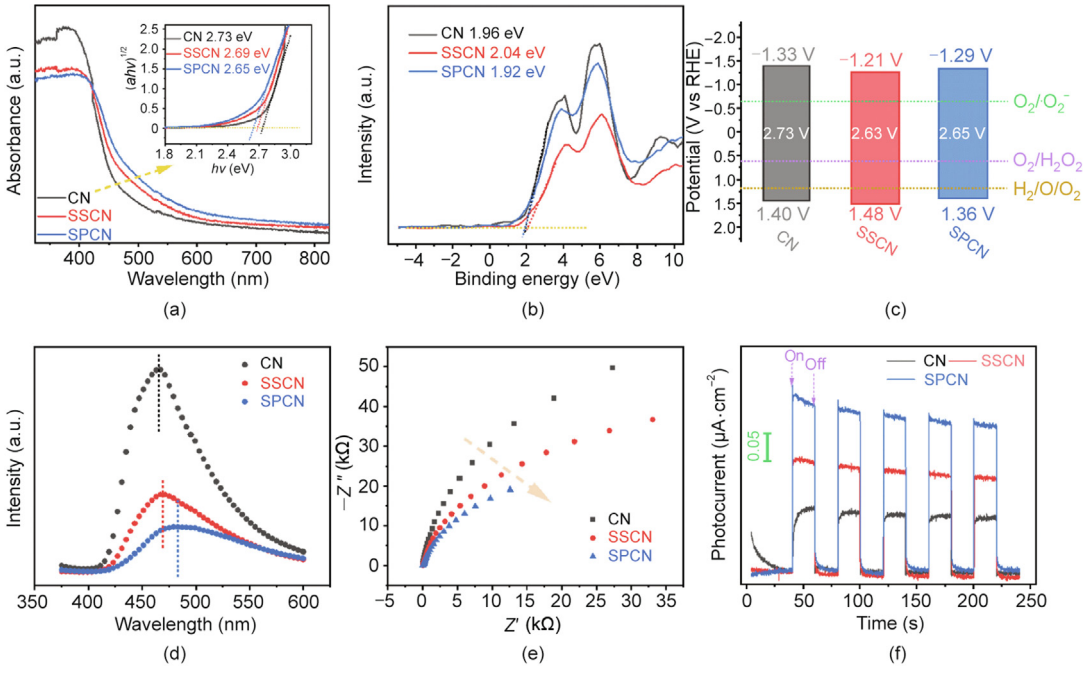

Fig. 3. Optical properties and electronic band structure of as-synthesized photocatalysts. (a) UV–vis DRS of the catalysts. Inset shows the corresponding plots of transformed Kubelka–Munk function $((\alpha h\nu)^{1/2}$, where α is the absorption coefficient, h is Planck constant and ν is the optical frequency) vs photon energy ($h\nu$). (b) The UPS spectrum of SPCN. (c) The band structure alignments, (d) PL spectra, (e) EIS Nyquist plots, and (f) transient photocurrent responses of the catalysts.

electrons in the nitrogen-deficient sites on the catalyst, it is easier to trap the photoinduced holes, which leads to the reduced spatial separation of the photoinduced carriers [50] (details of electrochemical and photoelectrochemical tests are shown in Text S3 in Appendix A).

3.4. Photocatalytic activity for H_2O_2 generation

Fig. 4(a) shows that the production of H_2O_2 increased linearly with time by different catalysts under visible light irradiation ($\lambda \geq 420$ nm). SPCN exhibits the highest photocatalytic activity (323.6 $\mu mol \cdot L^{-1} \cdot h^{-1} \cdot g^{-1}$) among the three catalysts. Comparatively, the production rate of SPCN was calculated to be 161.8 $\mu mol \cdot L^{-1} \cdot h^{-1}$ which is about 4.5-fold higher than that of CN. Compared with the performance of other CN-based photocatalysts in the literature (Table S2 in Appendix A), SPCN shows an outstanding photocatalytic H_2O_2 generation rate. The produced H_2O_2 can also be effectively activated by carbon nitride under visible light irradiation to generate hydroxyl radicals (·OH) [21]. Hence, the overall H_2O_2 production rate represents the dynamic competition between the rates of formation (k_f, $\mu mol \cdot L^{-1} \cdot min^{-1}$) and decomposition ($k_d$, min^{-1}). The rate constants of k_f (zero-order kinetics) and k_d (first-order kinetics) were calculated by fitting the H_2O_2 evolution data shown in Fig. S6(a) in Appendix A into the formula (t represents the irradiation accumulation time) :

$$[H_2O_2] = (k_f/k_d)/[1 - \exp(k_d t)] \quad (1)$$

As shown in Fig. S6(b) in Appendix A, the k_f and k_d of SPCN were 3.05 $\mu mol \cdot L^{-1} \cdot min^{-1}$ and 0.0043 min^{-1}, respectively. Interestingly, SPCN exhibited the lowest k_d value, implying that the decomposition of H_2O_2 was hindered. This is possibly due to the improvement in the band edge positions of SPCN. The photoexcited electrons in the conduction band were not negative enough to cause the fast decomposition of the generated H_2O_2, described in Eq. (2).

$$H_2O_2 + e^- \rightarrow {}^{\cdot}OH + OH^- \quad (2)$$

From Fig. 4(b), the effects of oxygen on H_2O_2 production were studied. The H_2O_2 yield was suppressed from 161.8 $\mu mol \cdot L^{-1} \cdot h^{-1}$ in the air to 52.7 $\mu mol \cdot L^{-1} \cdot h^{-1}$ in the argon environment. In contrast, the production of H_2O_2 increases to 194.7 $\mu mol \cdot L^{-1} \cdot h^{-1}$ with pure O_2 gas purging. Therefore, the H_2O_2 production rate was significantly enhanced under the saturated O_2 condition, suggesting that O_2 plays a critical positive role in the reaction.

The impact of electron donors on photocatalytic H_2O_2 production was also investigated. As shown in Fig. S7(a) in Appendix A, the H_2O_2 production performance in the presence of electron donors was in the order of IPA (161.8 $\mu mol \cdot L^{-1} \cdot h^{-1}$) > MeOH (122.0 $\mu mol \cdot L^{-1} \cdot h^{-1}$) > EtOH (103.1 $\mu mol \cdot L^{-1} \cdot h^{-1}$) > deionized (DI) water (10.0 $\mu mol \cdot L^{-1} \cdot h^{-1}$). The MeOH and EtOH are typical sacrificial agents, which show similar negative effects on H_2O_2 production. In contrast, IPA is more conducive to selective H_2O_2 production than the two aliphatic alcohols. The electron donor can boost H_2O_2 production, which is in agreement with the results in previous studies [35,51]. In the case of DI water, the water oxidation reaction by photogenerated holes is slow, which leads to the recombination of photogenerated charges. Herein, IPA, as the electron donor, can promote photocatalytic H_2O_2 production by consuming the photogenerated holes. Besides, the yield of H_2O_2 decreases as the pH value increases from 5 to 7 (Fig. S7(b) in Appendix A). This is because the reduced proton concentration in the solution slows down the H_2O_2 production while increasing the H_2O_2 decomposition rate [52]. The stability and cycle performance of photocatalyst is essential for practical application. As shown in Fig. S8 in Appendix A, SPCN maintains 89.4 % of the initial H_2O_2 production performance after four cycles of reaction, confirming the good stability of SPCN for continuous photoproduction of H_2O_2. We further studied the H_2O_2 production under continuous irradiation for 7 h (Fig. 4(c)), and the SPCN showed a high accumulation of produced H_2O_2. The generated H_2O_2 is stable and its concentration has remained under dark conditions for more than 30 hours, which makes it a promising method of *in-situ* H_2O_2 generation for practical applications.

3.5. Reaction pathway of H_2O_2 generation

To study the reaction pathway of H_2O_2 evolution, the catalytic activities of CN, SSCN, and SPCN for oxygen reduction reaction (ORR) were studied using electrochemical voltammetry. Fig. S9 in Appendix A shows the linear sweep voltammetry (LSV) curves of the catalysts on a rotating disk electrode (RDE). The higher current densities were achieved from the SSCN and SPCN compared with that of CN at the same rotating speed, which suggests a higher cathodic ORR performance [4]. Based on the voltammetry results, the corresponding Koutecky–Levich (K–L) plots are obtained (Fig. 5(a)). The electron transfer numbers (n) of CN, SSCN, and SPCN, extracted from the slopes via the K–L analysis, are 1.41, 1.54, and 1.58, respectively. These values indicated that the oxygen reduction reactions on the catalysts have a mixed one- and two-electron pathways [53]. Among them, SPCN shows the highest n value, indicating the highest selectivity toward two-electron transfer for the H_2O_2 evolution. The one- and two-electron reactions can be specifically expressed as:

One-electron reaction:

$$O_2 + e^- \rightarrow {}^{\cdot}O_2^- \quad (3)$$

Two-electron reaction:

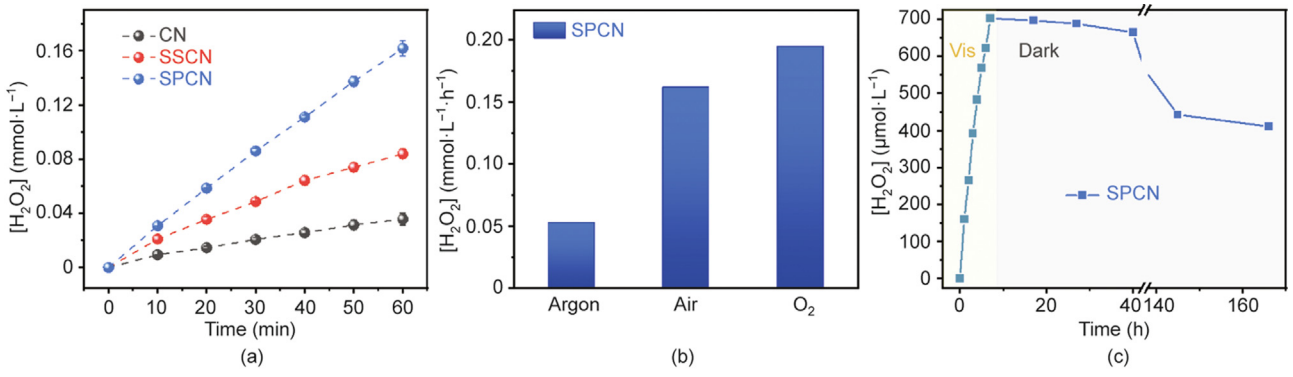

Fig. 4. Photocatalytic activity of H_2O_2 production. (a) The photocatalytic performance in H_2O_2 production with different photocatalysts. (b) Effect of dissolved oxygen on the photocatalytic production of H_2O_2. (c) Long-term photocatalytic H_2O_2 production under visible light and dark conditions. Working condition: 0.5 $g \cdot L^{-1}$ catalyst suspension, 50 ml IPA/H_2O mixture (10/90, v/v), pH 3.0, $\lambda \geq 420$ nm.

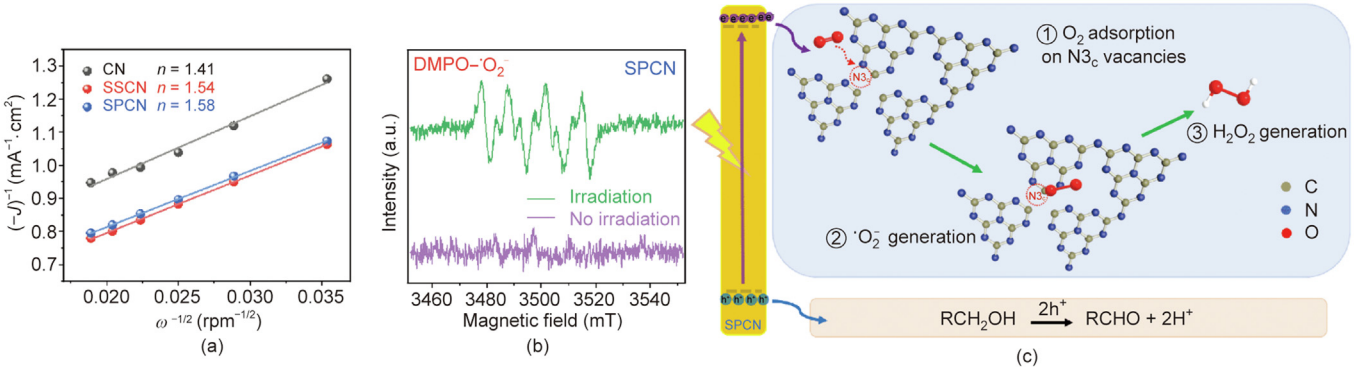

Fig. 5. Reaction pathway of photocatalytic reduction of O_2 to H_2O_2. (a) K–L plots of CN, SSCN, and SPCN were obtained from RDE results (J: the tested current density; ω: rotate speed; rpm: rotation per minute). (b) EPR signals of DMPO–$^{\cdot}O_2^-$ with SPCN under visible light irradiation. (c) Schematic diagram of efficient visible-light-driven H_2O_2 conversion by SPCN with $N3_C$ vacancies.

$$O_2 + 2e^- + 2H^+ \rightarrow H_2O_2 \quad (4)$$

The H_2O_2 evolution reaction involves oxygen, proton, and photoexcited electron, as described in Reaction (4) [2]. For the one-electron oxygen reduction, O_2 took an electron to produce $^{\cdot}O_2^-$. Then, the $^{\cdot}O_2^-$ combines another electron and two protons to convert to H_2O_2. To identify this photocatalytic O_2 reduction process, *p*-BQ and $AgNO_3$ were used as the chemical quenching agents to scavenge O_2^- and e^-, respectively [12]. Fig. S10 in Appendix A shows that when *p*-BQ or $AgNO_3$ were added into the photocatalytic reaction, the generation of H_2O_2 was completely suppressed.

The characteristic EPR signals of 5,5-dimethyl-1-pyrroline *N*-oxide (DMPO)–$^{\cdot}O_2^-$ were collected from SPCN as photocatalyst under visible light irradiation, shown in Fig. 5(b). The results suggest that O_2 was reduced to $^{\cdot}O_2^-$ via photoexcited electrons and $^{\cdot}O_2^-$ is the indispensable intermediate for photocatalytic H_2O_2 generation [54]. On the other hand, SPCN and SSCN have higher negative zeta potentials compared with CN, suggesting the higher adsorption capacity of H^+ which also promotes the generation of H_2O_2. Although SPCN exhibited a slightly positive zeta potential than SSCN at the same pH, the electron transfer number (n) of SPCN was higher than that of SSCN, indicating that $N3_C$ vacancies in SPCN dominated the contribution to the higher activity for H_2O_2 generation. Moreover, the oxygen adsorption capacity of the catalysts was evaluated by O_2-TPD experiments (Fig. S11 in Appendix A). The physisorption of O_2 is important in the initial stage of ORR. The TPD results show that SPCN has the highest physical O_2 adsorption capacity (< 200 °C) [55], which is because O_2 is more likely to be adsorbed on the C sites near the $N3_C$ vacancies [31].

Based on the above analysis, we propose a reaction pathway for the production of H_2O_2 by SPCN in Fig. 5(c). At first, O_2 molecules were adsorbed onto the C sites around N3c vacancies. With the illumination of visible light, SPCN generates electron-hole pairs. Due to the synergistic effect between the N3c vacancies and cyano group, SPCN offered excellent charge separation ability, which enables the efficient reduction of O_2 to $^{\cdot}O_2^-$. Finally, the $^{\cdot}O_2^-$ took another electron and reacted with the adsorbed H^+ to form H_2O_2.

4. Conclusions

In this study, we design a modified polymeric carbon nitride with rich $N3_C$ vacancies by sodium persulfate eutectic polymerization with melamine. The formation mechanism of nitrogen vacancies and other defects during the co-polymerization process is investigated, in which the $N3_C$ vacancies are formed by the persulfate-assisted molten polymerization process. The results show that SPCN with a high amount of $N3_C$ vacancies exhibits enhanced visible light absorption with accelerated photoexcited charge carrier separation compared with the unmodified CN. The SPCN shows excellent photocatalytic kinetic performance with high k_f (3.05 μmol·L^{-1}·min^{-1}) and low k_d (0.0043 min^{-1}) and delivers a 4.5-fold enhancement in H_2O_2 production (323.6 μmol·L^{-1}·h^{-1}·g^{-1}) compared to that of pristine CN. This work reveals insights into the high photocatalytic activity of $N3_C$ vacancies in photocatalytic H_2O_2 generation and offers a new perspective for the development of defect engineering in carbon nitride towards various photocatalytic applications.

Acknowledgments

This work was supported by the National Key Research and Development Program of China (2019YFC1905400).

Compliance with ethics guidelines

Wei Miao, Yijie Wang, Ying Liu, Hehe Qin, Chengcheng Chu, and Shun Mao declare that they have no conflict of interest or financial conflicts to disclose.

Appendix A. Supplementary data

Supplementary data to this article can be found online at https://doi.org/10.1016/j.eng.2021.12.016.

References

[1] Edwards JK, Solsona B, Ntainjua EN, Carley AF, Herzing AA, Kiely CJ, et al. Switching off hydrogen peroxide hydrogenation in the direct synthesis process. Science 2009;323(5917):1037–41.
[2] Lu Z, Chen G, Siahrostami S, Chen Z, Liu K, Xie J, et al. High-efficiency oxygen reduction to hydrogen peroxide catalysed by oxidized carbon materials. Nat Catal 2018;1:156–62.
[3] Su H, Christodoulatos C, Smolinski B, Arienti P, O'Connor G, Meng X. Advanced oxidation process for DNAN using UV/H_2O_2. Engineering 2019;5(5):849–54.
[4] Fan W, Zhang B, Wang X, Ma W, Li D, Wang Z, et al. Efficient hydrogen peroxide synthesis by metal-free polyterthiophene via photoelectrocatalytic dioxygen reduction. Energy Environ Sci 2020;13:238–45.
[5] Xia C, Xia Y, Zhu P, Fan L, Wang H. Direct electrosynthesis of pure aqueous H_2O_2 solutions up to 20% by weight using a solid electrolyte. Science 2019;366(6462):226–31.
[6] Sun Y, Han L, Strasser P. A comparative perspective of electrochemical and photochemical approaches for catalytic H_2O_2 production. Chem Soc Rev 2020;49(18):6605–31.
[7] Wang X, Wang F, Sang Y, Liu H. Full-spectrum solar-light-activated photocatalysts for light–chemical energy conversion. Adv Energy Mater 2017;7(23):1700473.
[8] Kormann C, Bahnemann DW, Hoffmann MR. Photocatalytic production of hydrogen peroxides and organic peroxides in aqueous suspensions of titanium dioxide, zinc oxide, and desert sand. Environ Sci Technol 1988;22(7):798–806.

[9] Tsukamoto D, Shiro A, Shiraishi Y, Sugano Y, Ichikawa S, Tanaka S, et al. Photocatalytic H_2O_2 production from ethanol/O_2 system using TiO_2 loaded with Au–Ag bimetallic alloy nanoparticles. ACS Catal 2012;2(4):599–603.
[10] Hirakawa H, Shiota S, Shiraishi Y, Sakamoto H, Ichikawa S, Hirai T. Au nanoparticles supported on $BiVO_4$: effective inorganic photocatalysts for H_2O_2 production from water and O_2 under visible light. ACS Catal 2016;6(8):4976–82.
[11] Isaka Y, Kondo Y, Kawase Y, Kuwahara Y, Mori K, Yamashita H. Photocatalytic production of hydrogen peroxide through selective two-electron reduction of dioxygen utilizing amine-functionalized MIL-125 deposited with nickel oxide nanoparticles. Chem Commun 2018;54(67):9270–3.
[12] Wu Q, Cao J, Wang X, Liu Y, Zhao Y, Wang H, et al. A metal-free photocatalyst for highly efficient hydrogen peroxide photoproduction in real seawater. Nat Commun 2021;12:483.
[13] Hou H, Zeng X, Zhang X. Production of hydrogen peroxide by photocatalytic processes. Angew Chem Int Ed Engl 2020;59(40):17356–76.
[14] Shiraishi Y, Takii T, Hagi T, Mori S, Kofuji Y, Kitagawa Y, et al. Resorcinol-formaldehyde resins as metal-free semiconductor photocatalysts for solar-to-hydrogen peroxide energy conversion. Nat Mater 2019;18(9):985–93.
[15] Xie H, Zheng Y, Guo X, Liu Y, Zhang Z, Zhao J, et al. Rapid microwave synthesis of mesoporous oxygen-doped g-C_3N_4 with carbon vacancies for efficient photocatalytic H_2O_2 production. ACS Sustain Chem Eng 2021;9(19):6788–98.
[16] Wu L, An S, Song YF. Heteropolyacids-immobilized graphitic carbon nitride: highly efficient photo-oxidation of benzyl alcohol in the aqueous phase. Engineering 2021;7(1):94–102.
[17] Qian X, Wu Y, Kan M, Fang M, Yue D, Zeng J, et al. FeOOH quantum dots coupled g-C_3N_4 for visible light driving photo-Fenton degradation of organic pollutants. Appl Catal B 2018;237:513–20.
[18] Zhang J, Jing B, Tang Z, Ao Z, Xia D, Zhu M, et al. Experimental and DFT insights into the visible-light driving metal-free C_3N_5 activated persulfate system for efficient water purification. Appl Catal B 2021;289:120023.
[19] Goclon J, Winkler K. Computational insight into the mechanism of O_2 to H_2O_2 reduction on amino-groups-containing g-C_3N_4. Appl Surf Sci 2018;462:134–41.
[20] Kumar A, Raizada P, Hosseini-Bandegharaei A, Thakur VK, Nguyen VH, Singh P. C-, N-vacancy defect engineered polymeric carbon nitride towards photocatalysis: viewpoints and challenges. J Mater Chem A Mater Energy Sustain 2021;9:111–53.
[21] Yang C, Xue Z, Qin J, Sawangphruk M, Zhang X, Liu R. Heterogeneous structural defects to prompt charge shuttle in g-C_3N_4 plane for boosting visible-light photocatalytic activity. Appl Catal B 2019;259:118094.
[22] Yu H, Shi R, Zhao Y, Bian T, Zhao Y, Zhou C, et al. Alkali-assisted synthesis of nitrogen deficient graphitic carbon nitride with tunable band structures for efficient visible-light-driven hydrogen evolution. Adv Mater 2017;29(16):1605148.
[23] Tian J, Wang D, Li S, Pei Y, Qiao M, Li ZH, et al. KOH-assisted band engineering of polymeric carbon nitride for visible light photocatalytic oxygen reduction to hydrogen peroxide. ACS Sustain Chem Eng 2020;8(1):594–603.
[24] Zhang G, Lin L, Li G, Zhang Y, Savateev A, Zafeiratos S, et al. Ionothermal synthesis of triazine-heptazine-based copolymers with apparent quantum yields of 60% at 420 nm for solar hydrogen production from "sea water." Angew Chem Int Ed Engl 2018;57(30):9372–6.
[25] Moon G, Fujitsuka M, Kim S, Majima T, Wang X, Choi W. Eco-friendly photochemical production of H_2O_2 through O_2 reduction over carbon nitride frameworks incorporated with multiple heteroelements. ACS Catal 2017;7(4):2886–95.
[26] Zhang P, Tong Y, Liu Y, Vequizo JJM, Sun H, Yang C, et al. Heteroatom dopants promote two-electron O_2 reduction for photocatalytic production of H_2O_2 on polymeric carbon nitride. Angew Chem Int Ed 2020;59(37):16209–17.
[27] Wu S, Yu H, Chen S, Quan X. Enhanced Photocatalytic H_2O_2 production over carbon nitride by doping and defect engineering. ACS Catal 2020;10(24):14380–9.
[28] Feng C, Tang L, Deng Y, Wang J, Luo J, Liu Y, et al. Synthesis of leaf-vein-like g-C_3N_4 with tunable band structures and charge transfer properties for selective photocatalytic H_2O_2 evolution. Adv Funct Mater 2020;30(39):2001922.
[29] Xie Y, Li Y, Huang Z, Zhang J, Jia X, Wang XS, et al. Two types of cooperative nitrogen vacancies in polymeric carbon nitride for efficient solar-driven H_2O_2 evolution. Appl Catal B 2020;265:118581.
[30] Nguyen CC, Do TO. Engineering the high concentration of $N3_C$ nitrogen vacancies toward strong solar light-driven photocatalyst-based g-C_3N_4. ACS Appl Energy Mater 2018;1(9):4716–23.
[31] Duan Y, Wang Y, Gan L, Meng J, Feng Y, Wang K, et al. Amorphous carbon nitride with three coordinate nitrogen ($N3_C$) vacancies for exceptional NO_x abatement in visible light. Adv Energy Mater 2021;11(19):2004001.
[32] Furukawa S, Shishido T, Teramura K, Tanaka T. Photocatalytic oxidation of alcohols over TiO_2 covered with Nb_2O_5. ACS Catal 2012;2(1):175–9.
[33] Miao W, Liu Y, Chen X, Zhao Y, Mao S. Tuning layered Fe-doped g-C_3N_4 structure through pyrolysis for enhanced fenton and photo-fenton activities. Carbon 2020;159:461–70.
[34] Yuan D, Ding J, Zhou J, Wang L, Wan H, Dai WL, et al. Graphite carbon nitride nanosheets decorated with ZIF-8 nanoparticles: effects of the preparation method and their special hybrid structures on the photocatalytic performance. J Alloys Compd 2018;762:98–108.
[35] Zhang H, Jia L, Wu P, Xu R, He J, Jiang W. Improved H_2O_2 photogeneration by KOH-doped g-C_3N_4 under visible light irradiation due to synergistic effect of N defects and K modification. Appl Surf Sci 2020;527:146584.
[36] Shen JS, Cai QG, Jiang YB, Zhang HW. Anion-triggered melamine based self-assembly and hydrogel. Chem Commun 2010;46:6786–8.
[37] Huang ZF, Song J, Pan L, Wang Z, Zhang X, Zou JJ, et al. Carbon nitride with simultaneous porous network and O-doping for efficient solar-energy-driven hydrogen evolution. Nano Energy 2015;12:646–56.
[38] Dong F, Ou M, Jiang Y, Guo S, Wu Z. Efficient and durable visible light photocatalytic performance of porous carbon nitride nanosheets for air purification. Ind Eng Chem Res 2014;53(6):2318–30.
[39] Chen Z, Sun P, Fan B, Liu Q, Zhang Z, Fang X. Textural and electronic structure engineering of carbon nitride via doping with π-deficient aromatic pyridine ring for improving photocatalytic activity. Appl Catal B 2015;170–171:10–6.
[40] Shi L, Yang L, Zhou W, Liu Y, Yin L, Hai X, et al. Photoassisted construction of holey defective g-C_3N_4 photocatalysts for efficient visible-light-driven H_2O_2 production. Small 2018;14(9):1703142.
[41] Cheng J, Hu Z, Lv K, Wu X, Li Q, Li Y, et al. Drastic promoting the visible photoreactivity of layered carbon nitride by polymerization of dicyandiamide at high pressure. Appl Catal B 2018;232:330–9.
[42] Miao W, Liu Y, Wang D, Du N, Ye Z, Hou Y, et al. The role of Fe–N_x single-atom catalytic sites in peroxymonosulfate activation: formation of surface-activated complex and non-radical pathways. Chem Eng J 2021;423:130250.
[43] Savateev A, Pronkin S, Epping JD, Willinger MG, Wolff C, Neher D, et al. Potassium poly(heptazine imides) from aminotetrazoles: shifting band gaps of carbon nitride-like materials for more efficient solar hydrogen and oxygen evolution. Chem Cat Chem 2017;9(1):167–74.
[44] Wang Y, Meng D, Zhao X. Visible-light-driven H_2O_2 production from O_2 reduction with nitrogen vacancy-rich and porous graphitic carbon nitride. Appl Catal B 2020;273:119064.
[45] Deng Y, Tang L, Zeng G, Zhu Z, Yan M, Zhou Y, et al. Insight into highly efficient simultaneous photocatalytic removal of Cr(VI) and 2,4-diclorophenol under visible light irradiation by phosphorus doped porous ultrathin g-C_3N_4 nanosheets from aqueous media: performance and reaction mechanism. Appl Catal B 2017;203:343–54.
[46] Zhu X, Yang J, Zhu X, Yuan J, Zhou M, She X, et al. Exploring deep effects of atomic vacancies on activating CO_2 photoreduction via rationally designing indium oxide photocatalysts. Chem Eng J 2021;422:129888.
[47] Liu J, Liu Y, Liu N, Han Y, Zhang X, Huang H, et al. Metal-free efficient photocatalyst for stable visible water splitting via a two-electron pathway. Science 2015;347(6225):970–4.
[48] Niu P, Yin LC, Yang YQ, Liu G, Cheng HM. Increasing the visible light absorption of graphitic carbon nitride (melon) photocatalysts by homogeneous self-modification with nitrogen vacancies. Adv Mater 2014;26(47):8046–52.
[49] Xiong J, Li X, Huang J, Gao X, Chen Z, Liu J, et al. CN/rGO@BPQDs high-low junctions with stretching spatial charge separation ability for photocatalytic degradation and H_2O_2 production. Appl Catal B 2020;266:118602.
[50] Liu Y, Xie C, Li H, Chen H, Zou T, Zeng D. Improvement of gaseous pollutant photocatalysis with WO_3/TiO_2 heterojunctional-electrical layered system. J Hazard Mater 2011;196:52–8.
[51] Zhang J, Zheng L, Wang F, Chen C, Wu H, Leghari SAK, et al. The critical role of furfural alcohol in photocatalytic H_2O_2 production on TiO_2. Appl Catal B 2020;269:118770.
[52] Wang R, Pan K, Han D, Jiang J, Xiang C, Huang Z, et al. Solar-driven H_2O_2 generation from H_2O and O_2 using earth-abundant mixed-metal oxide@carbon nitride photocatalysts. ChemSusChem 2016;9(17):2470–9.
[53] Zheng L, Su H, Zhang J, Walekar LS, Vafaei Molamahmood H, Zhou B, et al. Highly selective photocatalytic production of H_2O_2 on sulfur and nitrogen co-doped graphene quantum dots tuned TiO_2. Appl Catal B 2018;239:475–84.
[54] Wang D, Li Q, Miao W, Liu Y, Du N, Mao S. One-pot synthesis of ultrafine NiO loaded and Ti^{3+} *in-situ* doped TiO_2 induced by cyclodextrin for efficient visible-light photodegradation of hydrophobic pollutants. Chem Eng J 2020;402:126211.
[55] Chu C, Miao W, Li Q, Wang D, Liu Y, Mao S. Highly efficient photocatalytic H_2O_2 production with cyano and SnO_2 co-modified g-C_3N_4. Chem Eng J 2022;428:132531.